

# Driving skyrmions with low threshold current density in Pt/CoFeB thin film

Brindaban Ojha,<sup>1,\*</sup> Sougata Mallick,<sup>2,\*</sup> Sujit Kumar Panigrahy,<sup>2</sup> Minaxi Sharma,<sup>1</sup> André Thiaville,<sup>2</sup> Stanislas Rohart,<sup>2,†</sup> and Subhankar Bedanta<sup>1,‡</sup>

<sup>1</sup>*Laboratory for Nanomagnetism and Magnetic Materials (LNMM),  
School of Physical Sciences, National Institute of Science Education and Research (NISER),  
An OCC of Homi Bhabha National Institute (HBNI), Jatni 752050, Odisha, India*

<sup>2</sup>*Laboratoire de Physique des Solides, Université Paris-Saclay,  
CNRS UMR 8502, F-91405 Orsay Cedex, France*

(Dated: May 24, 2022)

Magnetic skyrmions are topologically stable spin swirling particle like entities which are appealing for next generation spintronic devices. The expected low critical current density for the motion of skyrmions makes them potential candidates for future energy efficient electronic devices. Several heavy metal/ferromagnetic (HM/FM) systems have been explored in the past decade to achieve faster skyrmion velocity at low current densities. In this context, we have studied Pt/CoFeB/MgO heterostructures in which skyrmions have been stabilized at room temperature (RT). It has been observed that the shape of the skyrmions are perturbed even by the small stray field arising from low moment magnetic tips while performing the magnetic force microscopy (MFM), indicating presence of low pinning landscape in the samples. This hypothesis is indeed confirmed by the low threshold current density to drive the skyrmions in our sample, at velocities of few  $\sim 10$ m/s.

Keywords: Perpendicular magnetic anisotropy, Dzyaloshinskii-Moriya interaction (DMI), skyrmions, thinfilm

## INTRODUCTION

Since the proposition of employing skyrmions (chiral textures obtained in material with broken inversion symmetry) in spintronic devices [1], a collective research effort has addressed the key aspects of this subject. Skyrmions are topologically protected since the spin configuration cannot be twisted continuously to another magnetic state with a different topological number [2, 3]. Further, their solitonic nature allow them to behave like particles under the influence of the electrical excitations. These properties make them promising candidates for logic and storage technology [1, 3–9]. Further, the thermal Brownian motion of skyrmions is intrinsically random, nonrepeatable, stochastic, and unpredictable, making them ideal candidates for random number generations towards potential applications in neuro-morphic and probabilistic computing [10–13]. In the experimental perspective, there are three major challenges: (i) stabilization of skyrmions at room temperature, (ii) deterministic nucleation of skyrmions, and (iii) efficient motion of skyrmions under spin Hall effect (SHE). Over the last decade, many experimental works [14–20] have been focused in the aforementioned directions to achieve the ambitious goal of skyrmion based device applications. However, controlled nucleation and motion of individual skyrmions in nanotracks with low power consumption still remains a challenge.

The topological states can emerge due to spin frustration in single-crystal or amorphous materials with large coordination number [21–26]. However, in the non-frustrated ordered ferromagnetic materials, the neighboring spins principally exhibit collinear ordering due to Heisenberg exchange interaction. Nevertheless, the

presence of large spin-orbit coupling and Dzyaloshinskii-Moriya interaction (DMI) due to broken symmetry can lead to stabilization of non-collinear spin textures viz. skyrmions [16–19, 27], since DMI lowers the texture energy and favors chirality. The most widely used combination of such system is a heterostructure of heavy metal (HM)/ferromagnet (FM)/oxide (O) [17–19]. For spintronics, this structure also enables spin-orbit torque (SOT) to efficiently manipulate the texture [14, 28]. Recent works have revealed that the skyrmions can be stabilized, nucleated, and driven using external magnetic field [18, 19], electrical field [29, 30], spin polarized current pulses [14, 18, 19, 31], local field gradient [32, 33], anisotropy gradient [34], etc. Nevertheless, a crucial criterion for device applications is to drive the skyrmions at low power. This makes materials with low pinning energy landscape indispensable. Different mechanisms (i.e. particle model based numerical analysis, current driven motion of skyrmion via nanotack, skyrmion defect interactions, etc. ) suggest that a skyrmion can move around a defect as well as get pinned depending on the pinning sites, applied current density, etc. [14, 35–37]. Further, it is well established that at lower current densities, the effect of pinning on magnetic textures is more relevant than at larger current densities [38, 39]. One way of optimizing material properties to minimize pinning is to use disordered systems [40]. However, in spite of several works in this field, the required threshold current density to drive the skyrmions is yet to reach the desired limit for real-life applications.

In this context, we chose the combination of Pt/Co<sub>40</sub>Fe<sub>40</sub>B<sub>20</sub>/MgO to investigate the current driven dynamics of the skyrmions under the influence of SOT. CoFeB has been selected due to presence of lower pin-

ning potential in comparison to polycrystalline FM layers (viz., Co, Fe, etc.) [19]. It has been reported that the intrinsically amorphous CoFeB crystallizes into bcc structure after annealing beyond 300°C. The presence of an amorphous (and subsequently crystallized bcc phase) maybe expected to lead to a low density structural defects acting as pinning sites in compared to conventional fcc textured 3d ferromagnetic materials [19, 41–45]. Brillouin light scattering (BLS) measurements [46–49] have been performed to quantify the DMI in the samples. We show that the threshold current density to drive the skyrmions is significantly lower than the existing literature.

## EXPERIMENTAL DETAILS

We have prepared Ta (5 nm)/Pt (6 nm)/Co<sub>40</sub>Fe<sub>40</sub>B<sub>20</sub> ( $t_{CoFeB}$ )/MgO (2 nm)/Ta (3 nm) heterostructure on thermally oxidized Si/SiO<sub>2</sub>(100 nm) substrates. The schematic of the sample structure is shown in Fig. 1(a). We choose SiO<sub>2</sub> 100 nm since it leads to better signal in the optical measurements [50]. A Ta seed layer has been chosen to promote the (111) growth of Pt as well as to reduce the strain between Pt and the substrate. We also use a 3 nm Ta on the top as a capping layer. The thickness of CoFeB has been varied between 1.5 to 1.9 nm. The samples are named as S1, S2, S3, S4 and S5 for  $t_{CoFeB} = 1.5, 1.6, 1.7, 1.75$  and  $1.9$  nm, respectively. The sample preparation was performed in a high-vacuum chamber consisting of sputtering and e-beam evaporators. The base pressure of the chamber was better than  $8 \times 10^{-8}$  mbar. Ta, Pt, and CoFeB layers were deposited using DC magnetron sputtering while e-beam evaporation technique was employed to prepare MgO. The substrate has been rotated with 10 rpm during deposition to improve uniformity of the layers. Further, for deposition of CoFeB the Ar flow was kept at 10 sccm which allows uniform growth of the thin film. The growth pressure and rate of deposition for CoFeB were  $8 \times 10^{-4}$  mbar and 0.01 nm/s, respectively. The roughness of the sample is observed to be 0.2 nm from AFM measurements. In order to promote the interfacial perpendicular magnetic anisotropy (PMA), all the samples were annealed *in-situ* at 600°C for 1 hour in vacuum ( $\sim 1 \times 10^{-7}$  mbar), after deposition. To quantify the spontaneous magnetization ( $M_s$ ) of the samples we have performed hysteresis measurements via a superconducting quantum interference device (SQUID) magnetometer. Microfabrication of the tracks and the contacts in the samples has been performed using a two-step electron beam lithography (EBL) and Ar ion etching. We deposited Ti (5 nm) and Au (50 nm) contact pads for transport measurements using e-beam evaporation. The imaging of skyrmions and their dynamics under the application of current has been performed by magnetic force microscopy (MFM) using

homemade CoCr/Cr tip coating, to minimize tip induced perturbations [31, 51, 52]. BLS measurements have been performed in Damon-Eshbach geometry [46–49] to quantify the interfacial DMI (iDMI) in the samples.

## RESULTS AND DISCUSSION

To investigate the crystalline nature of our samples we have performed XRD measurements for the samples S1 and S2. From GIXRD data, we obtained peaks with low intensity in both the samples at  $\sim 45^\circ$  and  $\sim 68^\circ$ , which are not present in the virgin substrate (see Fig. S1 in supplementary information). These peaks have been associated to CoFe bcc phase previously reported in the literature [43, 53, 54]. The MOKE measurements (shown in Fig. S2 in the supplementary information) confirm that the samples S1 and S2 are out-of-plane (OOP) magnetized while samples S3, S4 and S5 are in-plane (IP) magnetized. To get further insight about anisotropy we have deduced the effective anisotropy ( $K_{eff}$ ) constant using the relation  $K_{eff} = -\frac{1}{2}\mu_0 H_s M_s$  (negative sign indicates the IP anisotropy), where  $H_s$  and  $M_s$  are saturation field, and spontaneous magnetization, respectively. The calculation of  $H_s$  is shown in supplementary information (Fig. S3). The  $M_s$  value of S1-S5 is obtained to be  $1.25 \times 10^6$  A/m,  $1.27 \times 10^6$  A/m,  $1.25 \times 10^6$  A/m,  $1.24 \times 10^6$  A/m, and  $1.26 \times 10^6$  A/m, respectively.

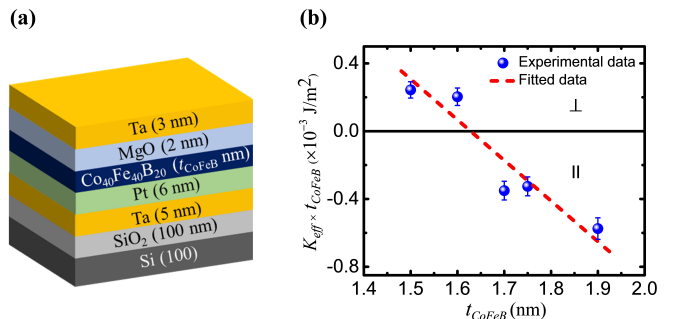


FIG. 1. (a) Schematic of sample structure. (b) Plot of  $K_{eff}t_{CoFeB}$  vs  $t_{CoFeB}$  and fit (red dashed line) using equation 1.

Fig. 1 (b) shows the plot of  $K_{eff}t_{CoFeB}$  vs  $t_{CoFeB}$ . The experimental data (blue dots) of this plot is fitted (red dashed line) using straight line fitting [49]:

$$K_{eff}t_{CoFeB} = K_V t_{CoFeB} + K_S \quad (1)$$

where  $K_V$  and  $K_S$  are volume and surface contributions of anisotropy, respectively. In fig. 1(b) the slope and intercept correspond to  $K_V$  and  $K_S$  which are  $-2.39$  MJ/m<sup>3</sup> and  $3.89$  mJ/m<sup>2</sup>, respectively. Here,  $K_V$  includes the shape anisotropy and  $K_S$  is the sum of two surface anisotropies arising from Pt/CoFeB and CoFeB/MgO interfaces. The best fit of Fig. 1(b) intersects the x-axis

at  $t_{\text{CoFeB}} = \sim 1.63$  nm depicting the occurrence of spin reorientation transition (SRT). We have performed the BLS measurements to quantify the iDMI of the samples. The detailed analysis of calculating the iDMI values from the BLS measurements is shown in the supplementary information. The iDMI constants are  $0.325 \pm 0.025$  mJ/m<sup>2</sup> and  $0.319 \pm 0.016$  mJ/m<sup>2</sup> for S1 and S2, respectively, which is similar to previous reports [47, 55].

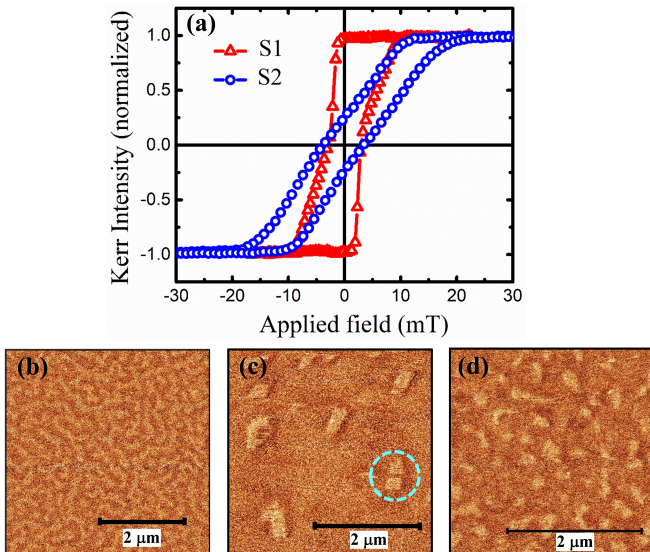


FIG. 2. (a) Hysteresis loop of sample S1 (red) and S2 (blue) in polar MOKE. (b) and (c) MFM images of sample S1 at demagnetized state and at an applied out-of-plane field of 1 mT, respectively. (d) MFM image of sample S2 at an applied field of 3 mT. The cyan circled area in (c) is a guide to the eye for the distorted shape of the skyrmion induced by tip perturbation (horizontal scanning).

In order to stabilize isolated skyrmions, we need to fine tune the DW energy [27] between two limiting cases: (a) a large positive energy which causes the collapse of the skyrmions, and (b) a large negative wall energy which destabilizes the collinear order, leading to isolated skyrmions only at large external magnetic field [31]. One way of achieving this is to keep the FM layer thickness near the SRT to reduce the effective anisotropy energy of the system to near zero. This is confirmed by the presence of skyrmionic states in samples S1 and S2 as observed using MFM. Fig. 2(a) shows the corresponding hysteresis loops of samples S1 (red curve) and S2 (blue curve). Wormlike stripe domains are observed in the demagnetized state indicating that the ground state is 1D textures (Fig. 2(b)). By applying OOP fields of 1 and 3 mT (Fig. 2(c) and (d)), isolated skyrmions have been observed in the samples S1, and S2, respectively. The average size of the skyrmions (measured within the accuracy of the MFM) varies in the range of 200-500 nm and 150-300 nm for samples S1 and S2, respectively. We note from fig. 2 (c), and (d) that the shape of the skyrmions

is significantly perturbed (for reference see cyan circled section of fig. 2(c)) even by the stray field of the lowest moment magnetic tips (a detailed discussion of the moment of the MFM tips and their effect on the magnetic textures is discussed in Fig. S6 of the supplementary information file). This indicates the presence of low pinning landscape in the CoFeB.

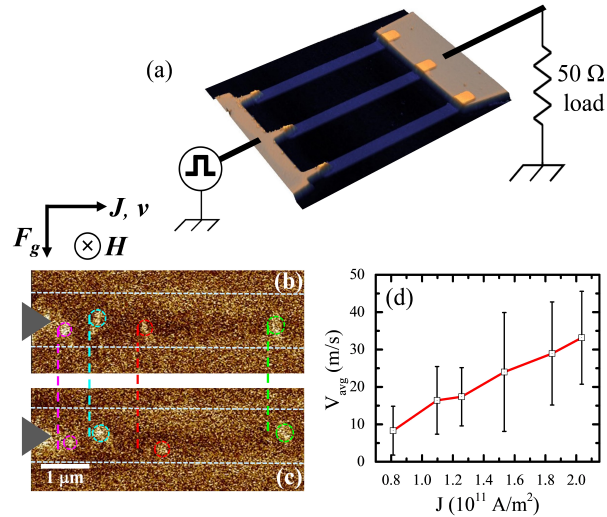


FIG. 3. (a) Schematic of the set-up for current induced motion experiment with the AFM image of three  $1\mu\text{m}$  wide nanotracks (blue) with Ti/Au contacts (light brown) microfabricated on sample S3 (CoFeB: 1.5 nm). (b) and (c) show the position (by coloured circles) and displacement (by coloured lines) of the skyrmions before and after application of one current pulse. The white dashed lines are indicating the boundary of a single nanotrack in the MFM image. Above these images, the arrows indicates the current  $J$ , velocity  $v$ , applied field  $H$  and gyrotropic deflection force  $F_g = G \times v$  (where  $G$  is the skyrmion gyrovector). (d) shows the average skyrmion velocity as a function of different applied current density.

Sample S1 is selected for the study of current-induced dynamics due to its lower pinning energy landscape and better control under applied magnetic field. We start from the demagnetized state and apply perpendicular magnetic field of 1.0 mT to stabilize the skyrmions in the tracks. Subsequently, we apply 19 ns current pulses with increasing amplitude. Fig. 3(a) shows the schematic of the sample structure with the AFM images of the nanotracks (3 parallel tracks with width  $\sim 1.2\mu\text{m}$  separated by  $\sim 2.8\mu\text{m}$  from each other) along with Ti/Au contact pads. The current is injected in the tracks using the point-like contacts on the left and collected at the common ground. Beyond a threshold current density of  $\sim 0.8 \times 10^{11}$  A/m<sup>2</sup>, the skyrmions start moving in the track. The motion of the skyrmions, opposite to the electron motion direction, confirms the dynamics due to SOT [14]. The skyrmion velocity as a function of applied current density is measured by calculating the average displacement of all the skyrmions present in the

TABLE I. Comparison of threshold current density with existing literature at room temperature. Two groups of results can be distinguished. In the first one, the measured velocities are well below 1 m/s, while in the second one, the velocities are larger than 10 m/s. In the second group, that concerns the fastest skyrmion, our work displays the smallest threshold current density.

Group	Authors	Sample structure	Threshold current density ( $\text{A}/\text{m}^2$ )	Velocity range (m/s)
1	Jiang <i>et al.</i> [18]	Ta/CoFeB/TaO <sub>x</sub>	$1.5 \times 10^8$	$(2.5 - 25) \times 10^{-6}$
	Yu <i>et al.</i> [56]	Ta/CoFeB/TaO <sub>x</sub>	$3.5 \times 10^9$	0.2 - 0.4
	Jiang <i>et al.</i> [57]	Ta/CoFeB/TaO <sub>x</sub>	$6 \times 10^9$	0.01 - 0.75
	Tolley <i>et al.</i> [58]	Ta/Pt/Co/Os/Pt/Ta	$2.0 \times 10^8$	$(2.5 - 13) \times 10^{-6}$
2	Woo <i>et al.</i> [19]	[Pt/Co/Ta] <sub>15</sub> ; [Pt/CoFeB/MgO] <sub>15</sub>	$2.0 \times 10^{11}$	1-45; 1-100
	Legrand <i>et al.</i> [59]	Ta/Co/[Pt/Ir/Co] <sub>10</sub> /Pt	$2.38 \times 10^{11}$	15 - 47
	Hrabec <i>et al.</i> [31]	Pt/FM/Au/FM/Pt, FM= Ni/Co/Ni	$2.6 \times 10^{11}$	10 - 60
	Woo <i>et al.</i> [60]	Ta/[Pt/CoFeB/MgO] <sub>20</sub> /Ta	$1.5 \times 10^{11}$	5 - 40
	Akhtar <i>et al.</i> [61]	Ta/Pt/CFA/MgO/Ta	$1.6 \times 10^{11}$	10
	Juge <i>et al.</i> [62]	Ta/Pt/Co/MgO/Ta	$3.5 \times 10^{11}$	15 - 100
	Litzius <i>et al.</i> [63]	[Pt/CoFeB/MgO] <sub>15</sub>	$3.2 \times 10^{11}$	1 - 35
	This work	Ta/Pt/CoFeB/MgO/Ta	$0.8 \times 10^{11}$	9 - 46

track. Fig. 3(b) and (c) show the skyrmion displacements marked by different colours before and after the application of one current pulse. It should be noted that both at lower as well as at higher current densities, the displacements of all the skyrmions are not equal. This is the consequence of the skyrmion hopping due to the presence of defects within the potential landscape [64]. The skyrmions advance in the track until they are either pinned or face strong skyrmion-skyrmion repulsion from another pinned skyrmion. We have plotted the average velocity of all the skyrmions present in the track for a particular current density (Fig. 3(d)). The error bar in Fig. 3(d) corresponds to the difference between highest and lowest skyrmion displacement. We obtain the highest skyrmion velocity of  $\sim 46$  m/s for a current density of  $\sim 2 \times 10^{11}$  A/m<sup>2</sup>. Application of higher current densities led to burning of the contacts due to application of large (19 ns) current pulses through the tracks (see Fig. S7 in supplementary information for details). The threshold current density reported in this work is lower than the ones reported in the literature (see Table 1), while giving access to velocities of few 10 m/s slightly above, among the best reports.

## CONCLUSIONS

In conclusion, we have shown that skyrmions are stabilized at very low field in Pt/CoFeB/MgO heterostructures at room temperature. We have quantified the iDMI value for our thin films which is similar to earlier reports. We observe significantly lower threshold current densities to drive the skyrmions. Larger skyrmion velocity under

shorter current pulses can be expected in similar samples. We believe that the work presented here may be helpful to utilize such low pinning materials for skyrmionic applications at low power consumption.

## ACKNOWLEDGMENTS

The authors thank DAE, Govt. of India and the Indo-French collaborative project supported by CEFIPRA (IFC/5808-1/2017), and the French National Research Agency (ANR) (Topsky, ANR-17-CE24-0025) for providing the research funding. The BLS setup was funded by the PhOM and EOE Research Departments of Université Paris-Saclay, CNRS-Institut de Physique, French National Research Agency (ANR) as part of the “Investissements d’Avenir” program (Labex NanoSaclay, ANR-10-LABX-0035) through the BLS@Psay and SPICY projects, and Ile-de-France region through the SESAME IMAGE SPIN (EX039175) project. We would like to thank Dr. Braj Bhusan Singh for the help in SQUID measurements and valuable discussion. We would also like to thank Raphael Weil for his help in microfabrication.

\* These authors contributed equally to this work

† [stanislas.rohart@universite-paris-saclay.fr](mailto:stanislas.rohart@universite-paris-saclay.fr)

‡ [sbedanta@niser.ac.in](mailto:sbedanta@niser.ac.in)

- [1] A. Fert, V. Cros, and J. Sampaio, *Nature nanotechnology* **8**, 152 (2013).  
 [2] N. Nagaosa and Y. Tokura, *Nature nanotechnology* **8**, 899 (2013).

- [3] A. Fert, N. Reyren, and V. Cros, *Nature Reviews Materials* **2**, 17031 (2017).
- [4] W. Koshibae, Y. Kaneko, J. Iwasaki, M. Kawasaki, Y. Tokura, and N. Nagaosa, *Japanese Journal of Applied Physics* **54**, 053001 (2015).
- [5] R. Tomasello, E. Martinez, R. Zivieri, L. Torres, M. Carpentieri, and G. Finocchio, *Scientific reports* **4**, 6784 (2014).
- [6] G. Yu, P. Upadhyaya, X. Li, W. Li, S. K. Kim, Y. Fan, K. L. Wong, Y. Tserkovnyak, P. K. Amiri, and K. L. Wang, *Nano letters* **16**, 1981 (2016).
- [7] X. Zhang, G. Zhao, H. Fangohr, J. P. Liu, W. Xia, J. Xia, and F. Morvan, *Scientific reports* **5**, 7643 (2015).
- [8] W. Kang, Y. Huang, C. Zheng, W. Lv, N. Lei, Y. Zhang, X. Zhang, Y. Zhou, and W. Zhao, *Scientific reports* **6**, 23164 (2016).
- [9] S. Zhang, J. Wang, Q. Zheng, Q. Zhu, X. Liu, S. Chen, C. Jin, Q. Liu, C. Jia, and D. Xue, *New Journal of Physics* **17**, 023061 (2015).
- [10] D. Pinna, F. A. Araujo, J.-V. Kim, V. Cros, D. Querlioz, P. Bessière, J. Droulez, and J. Grollier, *Physical Review Applied* **9**, 064018 (2018).
- [11] J. Zázvorka, F. Jakobs, D. Heinze, N. Keil, S. Kromin, S. Jaiswal, K. Litzius, G. Jakob, P. Virnau, D. Pinna, et al., *Nature nanotechnology* **14**, 658 (2019).
- [12] Y. Yao, X. Chen, W. Kang, Y. Zhang, and W. Zhao, *IEEE Transactions on Electron Devices* **67**, 2553 (2020).
- [13] K. M. Song, J.-S. Jeong, B. Pan, X. Zhang, J. Xia, S. Cha, T.-E. Park, K. Kim, S. Finizio, J. Raabe, et al., *Nature Electronics* **3**, 148 (2020).
- [14] J. Sampaio, V. Cros, S. Rohart, A. Thiaville, and A. Fert, *Nature nanotechnology* **8**, 839 (2013).
- [15] D. Maccariello, W. Legrand, N. Reyren, K. Garcia, K. Bouzehouane, S. Collin, V. Cros, and A. Fert, *Nature nanotechnology* **13**, 233 (2018).
- [16] A. Soumyanarayanan, M. Raju, A. G. Oyarce, A. K. Tan, M.-Y. Im, A. Petrović, P. Ho, K. Khoo, M. Tran, C. Gan, et al., *Nature materials* **16**, 898 (2017).
- [17] O. Boulle, J. Vogel, H. Yang, S. Pizzini, D. de Souza Chaves, A. Locatelli, T. O. Mentes, A. Sala, L. D. Buda-Prejbeanu, O. Klein, et al., *Nature nanotechnology* **11**, 449 (2016).
- [18] W. Jiang, P. Upadhyaya, W. Zhang, G. Yu, M. B. Jungfleisch, F. Y. Fradin, J. E. Pearson, Y. Tserkovnyak, K. L. Wang, O. Heinonen, et al., *Science* **349**, 283 (2015).
- [19] S. Woo, K. Litzius, B. Krüger, M.-Y. Im, L. Caretta, K. Richter, M. Mann, A. Krone, R. M. Reeve, M. Weigand, et al., *Nature materials* **15**, 501 (2016).
- [20] Y. Zhou and M. Ezawa, *Nature communications* **5**, 4652 (2014).
- [21] E. Mendive-Tapia, M. dos Santos Dias, S. Grytsiuk, J. B. Staunton, S. Blügel, and S. Lounis, *Physical Review B* **103**, 024410 (2021).
- [22] C. T. Ma, Y. Xie, H. Sheng, A. W. Ghosh, and S. J. Poon, *Scientific reports* **9**, 9964 (2019).
- [23] X. Zhang, J. Xia, Y. Zhou, X. Liu, H. Zhang, and M. Ezawa, *Nature communications* **8**, 1717 (2017).
- [24] P. Sutcliffe, *Physical review letters* **118**, 247203 (2017).
- [25] R. Streubel, D. S. Bouma, F. Bruni, X. Chen, P. Ercius, J. Ciston, A. T. N'Diaye, S. Roy, S. D. Kevan, P. Fischer, et al., *Advanced Materials* **33**, 2004830 (2021).
- [26] X. Yu, Y. Tokunaga, Y. Taguchi, and Y. Tokura, *Advanced Materials* **29**, 1603958 (2017).
- [27] S. Rohart and A. Thiaville, *Physical Review B* **88**, 184422 (2013).
- [28] A. Thiaville, S. Rohart, É. Jué, V. Cros, and A. Fert, *EPL (Europhysics Letters)* **100**, 57002 (2012).
- [29] C. Ma, X. Zhang, J. Xia, M. Ezawa, W. Jiang, T. Ono, S. Piramanayagam, A. Morisako, Y. Zhou, and X. Liu, *Nano letters* **19**, 353 (2018).
- [30] M. Schott, A. Bernand-Mantel, L. Ranno, S. Pizzini, J. Vogel, H. Béa, C. Baraduc, S. Auffret, G. Gaudin, and D. Givord, *Nano letters* **17**, 3006 (2017).
- [31] A. Hrabec, J. Sampaio, M. Belmeguenai, I. Gross, R. Weil, S. M. Chérif, A. Stashkevich, V. Jacques, A. Thiaville, and S. Rohart, *Nature communications* **8**, 15765 (2017).
- [32] R. Tomasello, S. Komineas, G. Siracusano, M. Carpentieri, and G. Finocchio, *Physical Review B* **98**, 024421 (2018).
- [33] F. Büttner, C. Moutafis, M. Schneider, B. Krüger, C. Günther, J. Geilhufe, C. v. K. Schmising, J. Mohanty, B. Pfau, S. Schaffert, et al., *Nature Physics* **11**, 225 (2015).
- [34] A. Casiraghi, H. Corte-León, M. Vafaei, F. Garcia-Sanchez, G. Durin, M. Pasquale, G. Jakob, M. Kläui, and O. Kazakova, *Communications Physics* **2**, 145 (2019).
- [35] C. Reichhardt, D. Ray, and C. O. Reichhardt, *Physical review letters* **114**, 217202 (2015).
- [36] S.-Z. Lin, C. Reichhardt, C. D. Batista, and A. Saxena, *Physical Review B* **87**, 214419 (2013).
- [37] D. Stosic, T. B. Ludermir, and M. V. Milošević, *Physical Review B* **96**, 214403 (2017).
- [38] C. Hanneken, A. Kubetzka, K. Von Bergmann, and R. Wiesendanger, *New Journal of Physics* **18**, 055009 (2016).
- [39] C. Reichhardt and C. O. Reichhardt, *Reports on Progress in Physics* **80**, 026501 (2016).
- [40] J.-V. Kim and M.-W. Yoo, *Applied Physics Letters* **110**, 132404 (2017).
- [41] C. Burrowes, N. Vernier, J.-P. Adam, L. Herrera Diez, K. Garcia, I. Barisic, G. Agnus, S. Eimer, J.-V. Kim, T. Devolder, et al., *Applied Physics Letters* **103**, 182401 (2013).
- [42] S. Fukami, T. Suzuki, Y. Nakatani, N. Ishiwata, M. Yamanouchi, S. Ikeda, N. Kasai, and H. Ohno, *Applied Physics Letters* **98**, 082504 (2011).
- [43] S. Ikeda, K. Miura, H. Yamamoto, K. Mizunuma, H. Gan, M. Endo, S. Kanai, J. Hayakawa, F. Matsukura, and H. Ohno, *Nature materials* **9**, 721 (2010).
- [44] V. Uhlíř, J. Vogel, N. Rougemaille, O. Fruchart, Z. Ishaque, V. Cros, J. Camarero, J. Cezar, F. Sirotti, and S. Pizzini, *Journal of Physics: Condensed Matter* **24**, 024213 (2011).
- [45] S. Laribi, V. Cros, M. Munoz, J. Grollier, A. Hamzić, C. Deranlot, A. Fert, E. Martinez, L. López-Díaz, L. Vila, et al., *Applied physics letters* **90**, 232505 (2007).
- [46] M. Belmeguenai, J.-P. Adam, Y. Roussigné, S. Eimer, T. Devolder, J.-V. Kim, S. M. Cherif, A. Stashkevich, and A. Thiaville, *Physical Review B* **91**, 180405 (2015).
- [47] S. Tacchi, R. Troncoso, M. Ahlberg, G. Gubbiotti, M. Madami, J. Åkerman, and P. Landeros, *Physical review letters* **118**, 147201 (2017).
- [48] K. Di, V. L. Zhang, H. S. Lim, S. C. Ng, M. H. Kuok, X. Qiu, and H. Yang, *Applied Physics Letters* **106**,

- 052403 (2015).
- [49] M. Belmeguenai, Y. Roussigné, H. Bouloussa, S. Chérif, A. Stashkevich, M. Nasui, M. Gabor, A. Mora-Hernández, B. Nicholson, O.-O. Inyang, *et al.*, *Physical Review Applied* **9**, 044044 (2018).
- [50] A. Hrabec, M. Belmeguenai, A. Stashkevich, S. Chérif, S. Rohart, Y. Roussigné, and A. Thiaville, *Applied Physics Letters* **110**, 242402 (2017).
- [51] J.-Y. Chauleau, R. Weil, A. Thiaville, and J. Miltat, *Phys. Rev. B* **82**, 214414 (2010).
- [52] J. Torrejon, G. Malinowski, M. Pelloux, R. Weil, A. Thiaville, J. Curiale, D. Lacour, F. Montaigne, and M. Hehn, *Phys. Rev. Lett.* **109**, 106601 (2012).
- [53] J. Kanak, P. Wiśniowski, T. Stobiecki, A. Zaleski, W. Powroźnik, S. Cardoso, and P. Freitas, *Journal of Applied Physics* **113**, 023915 (2013).
- [54] T. Huang, X. Cheng, X. Guan, and X. Miao, *IEEE Transactions on Magnetism* **50**, 1 (2014).
- [55] R. Khan, P. Shepley, A. Hrabec, A. Wells, B. Ocker, C. Marrows, and T. Moore, *Applied Physics Letters* **109**, 132404 (2016).
- [56] G. Yu, P. Upadhyaya, Q. Shao, H. Wu, G. Yin, X. Li, C. He, W. Jiang, X. Han, P. K. Amiri, *et al.*, *Nano letters* **17**, 261 (2017).
- [57] W. Jiang, X. Zhang, G. Yu, W. Zhang, X. Wang, M. B. Jungfleisch, J. E. Pearson, X. Cheng, O. Heinonen, K. L. Wang, *et al.*, *Nature Physics* **13**, 162 (2017).
- [58] R. Tolley, S. Montoya, and E. Fullerton, *Physical Review Materials* **2**, 044404 (2018).
- [59] W. Legrand, D. Maccariello, N. Reyren, K. Garcia, C. Moutafis, C. Moreau-Luchaire, S. Collin, K. Bouzehouane, V. Cros, and A. Fert, *Nano letters* **17**, 2703 (2017).
- [60] S. Woo, K. M. Song, H.-S. Han, M.-S. Jung, M.-Y. Im, K.-S. Lee, K. S. Song, P. Fischer, J.-I. Hong, J. W. Choi, *et al.*, *Nature communications* **8**, 15573 (2017).
- [61] W. Akhtar, A. Hrabec, S. Chouaieb, A. Haykal, I. Gross, M. Belmeguenai, M. Gabor, B. Shields, P. Maletinsky, A. Thiaville, *et al.*, *Physical Review Applied* **11**, 034066 (2019).
- [62] R. Juge, S.-G. Je, D. de Souza Chaves, L. D. Buda-Prejbeanu, J. Peña-Garcia, J. Nath, I. M. Miron, K. G. Rana, L. Aballe, M. Foerster, *et al.*, *Physical Review Applied* **12**, 044007 (2019).
- [63] K. Litzius, J. Leliaert, P. Bassirian, D. Rodrigues, S. Kromin, I. Lemesch, J. Zazvorka, K.-J. Lee, J. Mulkers, N. Kerber, *et al.*, *Nature Electronics* **3**, 30 (2020).
- [64] K.-J. Kim, J.-C. Lee, S.-M. Ahn, K.-S. Lee, C.-W. Lee, Y. J. Cho, S. Seo, K.-H. Shin, S.-B. Choe, and H.-W. Lee, *Nature* **458**, 740 (2009).

# Supplementary Information

## Driving skyrmions with low threshold current density in Pt/CoFeB thin film

Brindaban Ojha,<sup>†,¶</sup> Sougata Mallick,<sup>‡,¶</sup> Sujit Kumar Panigrahy,<sup>‡</sup> Minaxi Sharma,<sup>†</sup> André Thiaville,<sup>‡</sup> Stanislas Rohart,<sup>\*,‡</sup> and Subhankar Bedanta<sup>\*,†</sup>

<sup>†</sup>*Laboratory for Nanomagnetism and Magnetic Materials (LNMM), School of Physical Sciences, National Institute of Science Education and Research (NISER), An OCC of Homi Bhabha National Institute (HBNI), Jatni 752050, Odisha, India*

<sup>‡</sup>*Laboratoire de Physique des Solides, Université Paris-Saclay, CNRS UMR 8502, F-91405 Orsay Cedex, France*

<sup>¶</sup>*These authors contributed equally to this work*

E-mail: stanislas.rohart@universite-paris-saclay.fr; sbedanta@niser.ac.in

# Sample characterization

## Structural characterization

Fig. S1 shows the GIXRD data of the samples S1 (CoFeB: 1.5 nm), S2 (CoFeB: 1.6 nm), and the bare substrate. We obtained peaks with low intensity in both the samples at  $45^\circ$  and  $68^\circ$  which have been associated to CoFe bcc phase.<sup>1-3</sup> The rather broad shape of the peaks are due to the low thickness of the thin films. The XRD measurements confirm amorphous to crystalline phase transformation of the CoFeB thin films due to annealing.

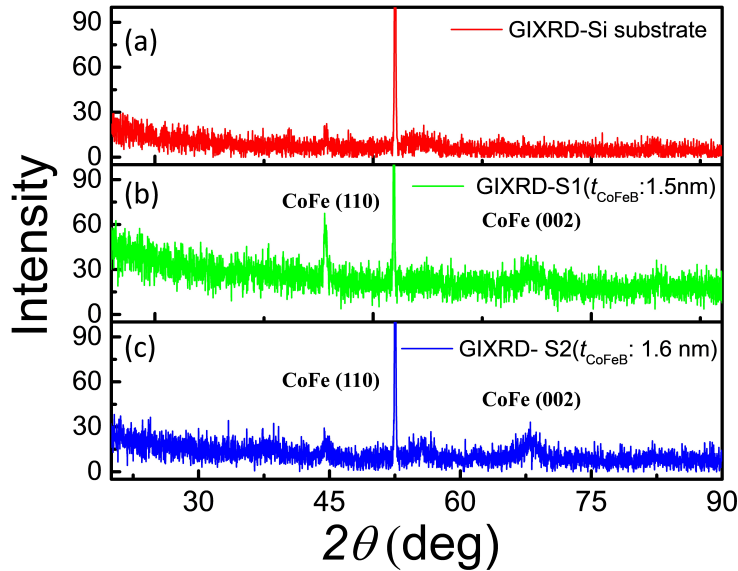


Figure S1: GIXRD measurements of the bare substrate and the samples S1 and S2 are shown in (a), (b) and (c), respectively. For proper comparison, the intensity axis scale is same for all the plots.

## Magnetometry

Fig. S2 shows the hysteresis loops of the samples measured by MOKE microscope. The easy axis of the magnetization of samples S1 and S2 (Fig. S2(a)) is oriented along out-of-plane (OOP) direction. The samples S3, S4 and S5 show an easy axis along in-plane (IP) direction (Fig. S2(b)).

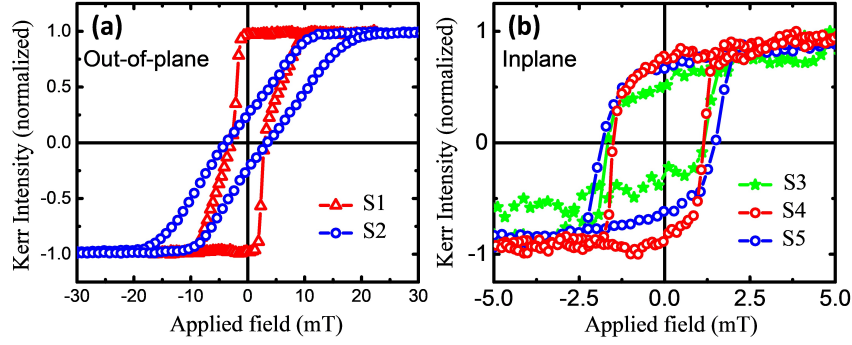


Figure S2: MOKE hysteresis loop for the samples S1 and S2 (a) and S3-S5 (b) measured at room temperature in polar and longitudinal modes, respectively.

$K_{eff}$  can be written as,  $K_{eff} = -\frac{1}{2}\mu_0 H_s M_s$  (negative sign indicates the IP anisotropy), where  $H_s$  and  $M_s$  are hard axis saturation field, and spontaneous magnetization, respectively.<sup>4</sup> Fig. S3 shows the hard axis hysteresis loops of all the samples measured via SQUID.

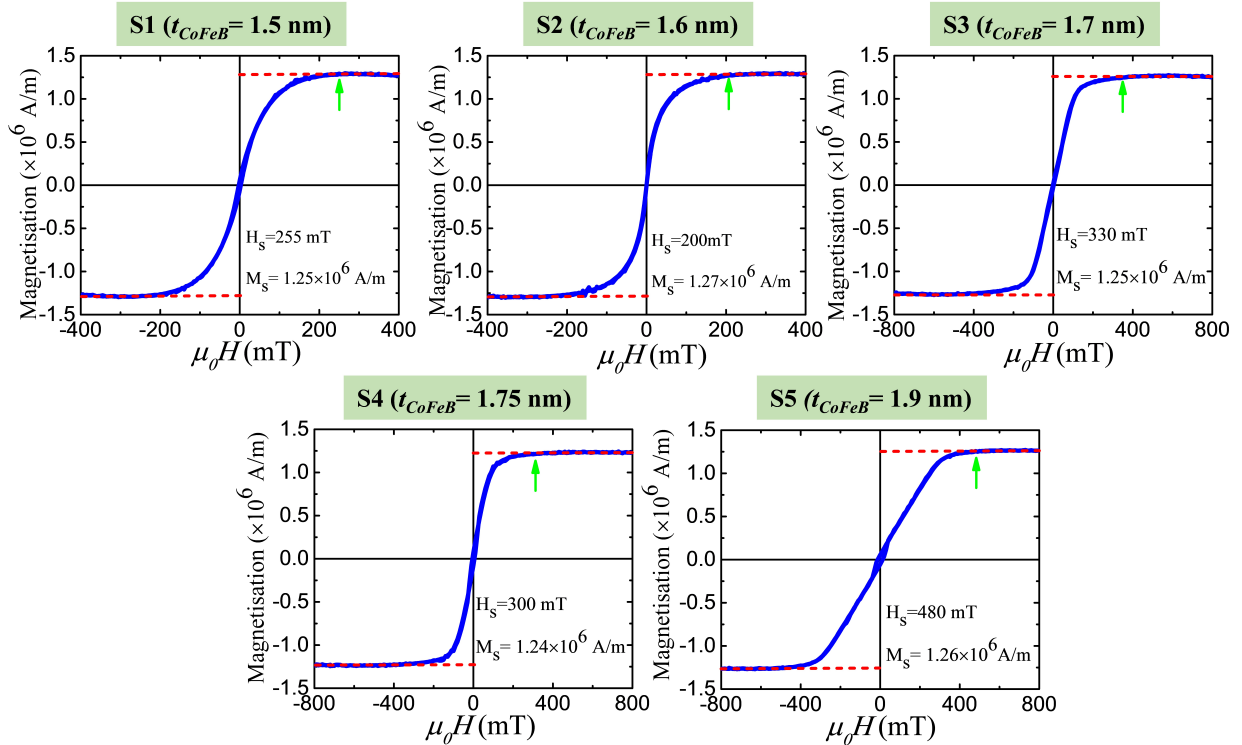


Figure S3: Hysteresis loops measured by SQUID for samples S1, S2, S3, S4 and S5. The green arrow sign in the plot represents the saturation field.

## iDMI measurement

Fig. (a) shows the schematic of the measurement geometry using Brillouin light scattering (BLS) in Damon Eshbach (DE) configuration. In this measurement, a horizontally polarized laser beam is incident on a sample surface where the incident photons interact with magnons. The  $180^\circ$  backscattered photons (arises due to inelastic scattering) are sent through a tandem Fabry-Perot (FP) interferometer to achieve a high spectral resolution and to extract the information about spin wave. Stokes (S) and Anti-stokes (AS) peaks arises due to creation and annihilation of the magnons, respectively, in the BLS spectra and the respective spin wave propagates in the opposite direction. The wave vector of the spin wave is represented as  $k_{sw} = \frac{4\pi \sin\theta}{\lambda}$ , where  $\theta$  is the incident angle, and  $\lambda$  ( $=532$  nm) is the wavelength of incident laser light. Here, a magnetic field has been applied perpendicular to the incident plane of light. Fig. S4 (b) shows the BLS spectra of the sample S2 measured at  $k_{sw} = 4.1 \mu\text{m}^{-1}$  and a constant applied field ( $\mu_0 H = 371$  mT).

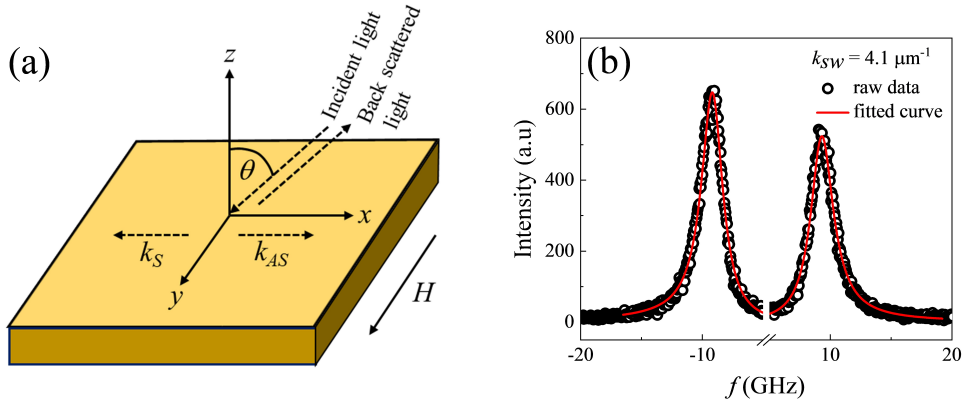


Figure S4: (a) Measurements geometry of BLS technique. (b) BLS spectra of sample S2 measured at a constant applied field ( $\mu_0 H = 371$  mT).

The BLS data have been analyzed using the following spin-wave dispersion relation in DE mode<sup>5-7</sup>

$$f = f_0 \pm f_{DMI} = \frac{\gamma \mu_0}{2\pi} \sqrt{[H + Jk_{sw}^2 + P(k_{sw})M_s][H + Jk_{sw}^2 - P(k_{sw})M_s - H_{K_{eff}}]} \pm \frac{\gamma}{\pi M_S} D_{eff} k_{sw} \quad (1)$$

where,  $\gamma$  is the absolute value of the gyromagnetic factor [ $\gamma/2\pi = g \times 13.996$  GHz/T, with  $g$  the gyromagnetic factor],  $\mu_0$  is the vacuum permeability,  $J = 2A/(\mu_0 M_S)$  is the SW stiffness constant with  $A$  the micromagnetic exchange constant,  $D_{eff}$  is the effective DMI constant,  $H_{K_{eff}}$  is the effective anisotropy,  $P(k_{sw}) = 1 - \frac{1 - \exp(-|k_{sw}|t_{CoFeB})}{|k_{sw}|t_{CoFeB}}$ . The first part of the above equation,  $f_0 = \frac{f_S + f_{AS}}{2}$  ( $f_S$  and  $f_{AS}$  peak frequencies of S and AS lines of BLS measurements), represents the average spin wave frequency having no iDMI at the HM/FM interface whereas the second part arises due to iDMI.

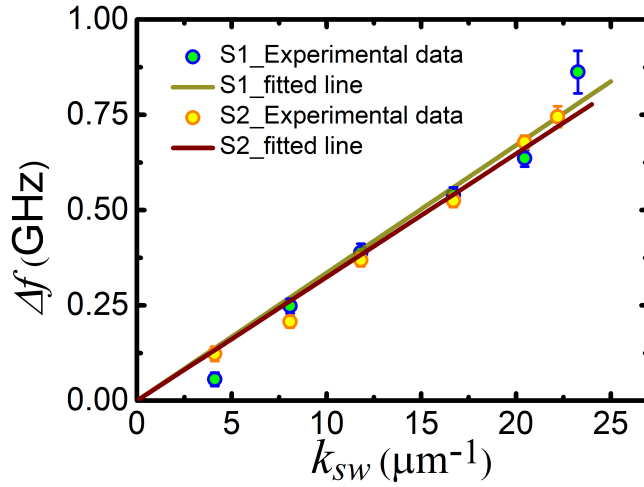


Figure S5: Plot of frequency difference ( $\Delta f$ ) vs spin wave vector ( $k_{sw}$ ) at  $\mu_0 H = 371$  mT

From equation (1) the frequency difference between S and AS peaks can be written as:

$$\Delta f = f_S - f_{AS} = \frac{2\gamma}{\pi M_S} D_{eff} k_{sw} \quad (2)$$

$\Delta f$  as a function of  $k_{sw}$  has been plotted in Fig. S5 for both the samples. From the slope of linear fit, DMI constant  $D_{eff}$  can be deduced. The magnitude of iDMI constants are  $0.325 \pm 0.025$  mJ/m<sup>2</sup> and  $0.319 \pm 0.016$  mJ/m<sup>2</sup> for S1 and S2, respectively.

# Magnetic force microscopy imaging

The MFM images were realized using two different microscope, a Bruker D3100 and a Park NX10 using two-pass scan, one for the topography and one at a higher distance (20 nm) to get the magnetic signal from the phase of the tip oscillation. In such a measurement, tip induced perturbation should occur during the topographic scan, when the tip to sample distance is the lowest. This is why we have used home-made tips that fix this problem. In addition to a magnetic coating (CoCr), we add a Cr capping layer. This last layer is not only meant to protect the magnetic coating but also increases the magnetic layer to sample distance during the topographic scan. This strategy has been successfully used in several of our studies<sup>8-10</sup> on magnetic solitons (skyrmions and domain walls) and prevent from dramatic and irreversible perturbations.

The consequences of the CoCr layer thickness on the images is shown in Fig. S6. In this figure we compare the same demagnetized state using two tips with CoCr(15 nm)/Cr(20 nm) [images (a) and (b)] and CoCr(5 nm)/Cr(20 nm) [image (c)] (same tip as in the manuscript). The striking difference between the two sets of images is that, contrary to the expected stripe state observed with the thinnest CoCr layer tip, the other tip shows more compact structures. This is the result of a significant perturbation which slices the stripes into more compact domains. Changing the scan direction between the  $x$  [image (a)] and  $y$  [image (b)] fast scan axis proves the perturbation since the observed textures are systematically elongated along the slow scan axis, probably due to a dragging effect by the magnetic tip. Note that if the thinnest CoCr layer tip produces minute perturbation on the stripe phase, the skyrmion state is still slightly perturbed [image (d) and main figures of the manuscript]. This behaviour is likely to be due to the low pinning landscape of the CoFeB thin films. Indeed, if we compare our previous study on Pt/Ni/Co/Ni/Au/Ni/Co/Ni/Pt layers hosting skyrmions,<sup>10</sup> skyrmions could even be imaged with a CoCr(15 nm)/Cr(20 nm) tip without noticeable perturbations.

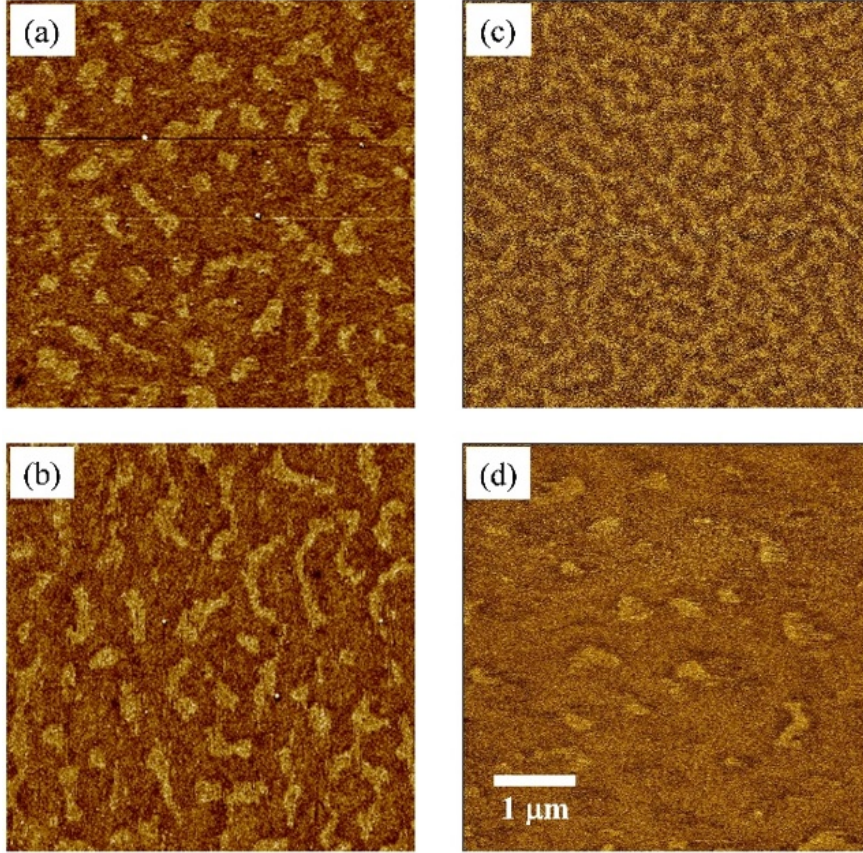


Figure S6: MFM image of the CoFeB sample in the demagnetized state (zero field) using a 15 nm/20 nm (a-b) and a 5 nm/20 nm (same tip as in the manuscript) (c) CoCr/Cr bilayers tip. Images (a) and (b) show significant perturbation whereas image (c) show the expected stripe phase. Note that the different scan direction (respectively  $x$  and  $y$  fast scan axis) between images (a) and (b) highlight the deformations due to the magnetic tips that show magnetic textures elongated along the slow scan axis. (d) Image obtained with a 3 mT applied field of the skyrmion state, using the 5 nm/20 nm (c) CoCr/Cr bilayers tip. This image shows that in the skyrmion phase, perturbation cannot be avoided. Thinner magnetic coating prevent from getting a good signal on the samples. The phase scale for all the three images are the same (300 mDeg). The image scales are identical, with a scale bar shown in (d).

## Current pulses

Current pulses through the sample through a  $50 \Omega$  impedance cable ended by a  $50 \Omega$  load to absorb the pulse power after transmission through the sample as shown in figure S7(a). Although this system can provide pulses raise time of about 100 ps, the high resistivity substrate significantly degraded the system respond time.

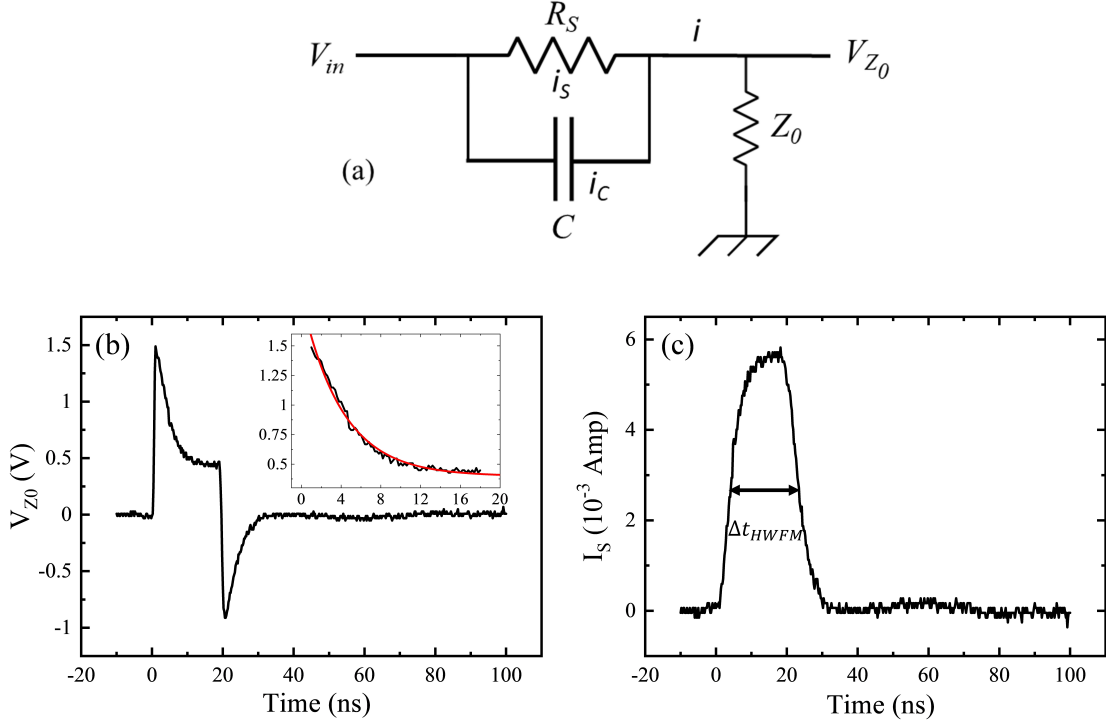


Figure S7: (a) Circuit diagram of the sample considering capacitive short through the substrate. (b) Shape of the voltage pulse measured on the  $50 \Omega$  load of an oscilloscope and (c) processed current pulse flowing through the nanotracks, for a 20 ns long 2 V pulse (note that due to the impedance mismatch at the sample, 25% of the pulse is reflected before the sample and does not participate to the pulse).

The substrate used in the experiment is a Si(001) substrate with a resistivity of  $0.01 \Omega \cdot \text{cm}$ , covered by 100 nm  $\text{SiO}_2$ . The oxide layer is sufficient to isolate the tracks in DC. However, since the substrate resistance is much lower than the track resistance  $R_S$ , the current initially flows through the substrate, due to capacitive coupling between the track leads and the substrate, through the  $\text{SiO}_2$  layer, as sketched in Fig. S7(a). The pulse measured on the  $50 \Omega$  load of an oscilloscope does not directly correspond to the current through the tracks, but to the sum of the currents through the substrate and the track. At the beginning of the pulse, the current flows directly through the capacitor and the voltage on the load is the one of the pulse. After the transient regime, the current through the capacitor is zero and the voltage on the load is  $Z_0/(Z_0 + R_S)$ . From the measurement in Fig. S7(b), a time constant of 4 ns and a track resistance  $R_S = 188 \Omega$  are deduced. The

current pulse through the sample can be deduced, as shown in Fig. S7(c). The pulse width is calculated as the full-width at full maxima of the pulse, here 19 ns. The current density through the sample is subsequently calculated by dividing the current with the product of width and thickness of the nanotracks.

## References

- (1) Ikeda, S.; Miura, K.; Yamamoto, H.; Mizunuma, K.; Gan, H.; Endo, M.; Kanai, S.; Hayakawa, J.; Matsukura, F.; Ohno, H. A perpendicular-anisotropy CoFeB–MgO magnetic tunnel junction. *Nature materials* **2010**, *9*, 721–724.
- (2) Kanak, J.; Wiśniowski, P.; Stobiecki, T.; Zaleski, A.; Powroźnik, W.; Cardoso, S.; Freitas, P. X-ray diffraction analysis and Monte Carlo simulations of CoFeB-MgO based magnetic tunnel junctions. *Journal of Applied Physics* **2013**, *113*, 023915.
- (3) Huang, T.; Cheng, X.; Guan, X.; Miao, X. Effect of Ultrathin Inserted Ag Layer on Perpendicular Magnetic Anisotropy of CoFeB Thin Film. *IEEE Transactions on Magnetics* **2014**, *50*, 1–4.
- (4) Yamanouchi, M.; Jander, A.; Dhagat, P.; Ikeda, S.; Matsukura, F.; Ohno, H. Domain structure in CoFeB thin films with perpendicular magnetic anisotropy. *IEEE magnetics letters* **2011**, *2*, 3000304–3000304.
- (5) Belmeguenai, M.; Adam, J.-P.; Roussigné, Y.; Eimer, S.; Devolder, T.; Kim, J.-V.; Cherif, S. M.; Stashkevich, A.; Thiaville, A. Interfacial Dzyaloshinskii-Moriya interaction in perpendicularly magnetized Pt/Co/AlO<sub>x</sub> ultrathin films measured by Brillouin light spectroscopy. *Physical Review B* **2015**, *91*, 180405.
- (6) Tacchi, S.; Troncoso, R.; Ahlberg, M.; Gubbiotti, G.; Madami, M.; Åkerman, J.; Landeros, P. Interfacial Dzyaloshinskii-Moriya interaction in Pt/CoFeB films: Effect of the heavy-metal thickness. *Physical review letters* **2017**, *118*, 147201.

- (7) Di, K.; Zhang, V. L.; Lim, H. S.; Ng, S. C.; Kuok, M. H.; Qiu, X.; Yang, H. Asymmetric spin-wave dispersion due to Dzyaloshinskii-Moriya interaction in an ultrathin Pt/CoFeB film. *Applied Physics Letters* **2015**, *106*, 052403.
- (8) Chauleau, J.-Y.; Weil, R.; Thiaville, A.; Miltat, J. Magnetic domain walls displacement: Automotion versus spin-transfer torque. *Phys. Rev. B* **2010**, *82*, 214414.
- (9) Torrejon, J.; Malinowski, G.; Pelloux, M.; Weil, R.; Thiaville, A.; Curiale, J.; Lacour, D.; Montaigne, F.; Hehn, M. Unidirectional Thermal Effects in Current-Induced Domain Wall Motion. *Phys. Rev. Lett.* **2012**, *109*, 106601.
- (10) Hrabec, A.; Sampaio, J.; Belmeguenai, M.; Gross, I.; Weil, R.; Chérif, S. M.; Stashkevich, A.; Jacques, V.; Thiaville, A.; Rohart, S. Current-induced skyrmion generation and dynamics in symmetric bilayers. *Nature communications* **2017**, *8*, 1–6.